A classical force field for selenium oxyanions in aqueous solutions and minerals

Artem A. Glushak[a], Evgeny V. Tararushkin[a], Grigory S. Smirnov[a]

[a]HSE University, Moscow, 101100, Russia

Abstract

Selenium species are highly soluble in water and also occur in cement structures. In this study, we develop a classical force field for selenate (SeO_4^{2-}) and selenite (SeO_3^{2-}) oxyanions. The force field is fitted to the *ab initio* calculations, including the hydrated properties and equilibrium geometries. It allows to study mobility of selenium ions in aqueous solutions and mineral nanopores using classical molecular dynamics.

Keywords: molecular dynamics, density functional theory, selenate, selenite

1. Introduction

Geological disposal allows the reliable isolation of radioactive waste, thereby protecting the natural environment from the effects of residual radiation [1, 2, 3]. Currently, clays and hardened cement are considered the best barrier materials due to their excellent sorption properties [4, 5]. The transport properties of the ^{79}Se isotope are considered for the safety assessment of waste repositories due to its long half-life.

Selenium tends to form oxyanions that are highly soluble in water. Four different oxidation states ($-II$, 0, IV, VI) of selenium are generally considered, and two of them (IV and VI) are of particular interest in the aqueous phase. According to the experimental data, selenite $Se(IV)O_3^{2-}$ and selenate $Se(VI)O_4^{2-}$ ions are also stable in the cement matrix [6, 7, 8]. While inner-sphere adsorption is observed for SeO_3^{2-} ions, SeO_4^{2-} ions mainly form outer sphere complexes at the interface of cement minerals [6, 7]. In addition, selenate could substitute sulfate ions in the AFm and AFt cement phases [6, 9, 8, 7].

Many experimental data on these anions have been published, both in the aqueous phases and at the interface of the minerals. At the same time, computational data are limited to quantum chemical-based methods due to the lack of the well-established selenium force field for classical molecular dynamics (MD) simulations. However, since classical MD modeling remains one of the main tools for studying the properties of barrier materials at the nanoscale, the creation of a force field for selenium oxyanions will significantly increase the possibilities of numerical studies [10, 11]. So far, we know one attempt to model a crystal with selenate ions using classical MD [12], but that interatomic potential lacks compatibility with other force

fields. Also, some parameters for selenium coincide with the sulfur parameters.

In this study, we develop an optimized classical force field for selenium oxyanions (SeO_4^{2-}, SeO_3^{2-}) based on the *ab initio* and experimental data. Our force field not only accurately describes the structural and dynamical properties of these ions in aqueous solutions, but also enables the modeling of selenate-containing mineral phases, as it is compatible with the ClayFF force field [13, 14]. ClayFF is a widely used non-polarized force field that allows the study of a wide range of natural and synthetic minerals, as well as their interaction with aqueous solutions [14].

2. Computational methods

2.1. Potential model

The analytical form of the proposed potential can be written as

$$U_{total} = U_{Coul} + U_{vdW} + U_{bond-stretch} + U_{bond-bend}, \quad (1)$$

where each component describes the corresponding interaction. The first two terms are interatomic. Coulomb potential describes the electrostatic interactions between the pairs of atoms:

$$U_{Coul} = \frac{q_i q_j}{r_{ij}} \quad (2)$$

where q_i and q_j are partial atomic charges, and r_{ij} is the distance between these atoms.

Van-der-Waals interactions are described by the Lennard-Jones (L-J) 12-6 potential:

$$U_{vdW} = 4\varepsilon_{ij} \left[\left(\frac{\sigma_{ij}}{r_{ij}} \right)^{12} - \left(\frac{\sigma_{ij}}{r_{ij}} \right)^6 \right] \quad (3)$$

Email addresses: `aglushak@hse.ru` (Artem A. Glushak), `evgeny.tararushkin@yandex.ru` (Evgeny V. Tararushkin), `g.smirnov@hse.ru` (Grigory S. Smirnov)

where ε_{ij} and σ_{ij} are L-J parameters. The interaction parameters between different atoms are obtained by Lorentz-Berthelot combining rules:

$$\sigma_{ij} = \frac{\sigma_i + \sigma_j}{2}, \varepsilon_{ij} = \sqrt{\varepsilon_i \varepsilon_j} \tag{4}$$

For water molecules we use the rigid SPC/E model [15], while L-J parameters for selenium oxyanions are optimized to reproduce their solvation energy in the classical MD simulations. The optimization process is discussed further.

The bonded interactions are described with the harmonic potentials

$$U_{bond-stretch} = \frac{1}{2} k_r (r_{ij} - r_{ij_0})^2 \tag{5}$$

$$U_{bond-bend} = \frac{1}{2} k_\theta (\theta_{ijk} - \theta_{ijk_0})^2 \tag{6}$$

where k_r, k_θ are force constants and r_0, θ_0 are the corresponding equilibrium bond lengths and angles. The values of these parameters are obtained from *ab initio* calculations.

We use the ClayFF force field with similar interactions [13, 14] to model the cement phases.

2.2. Ab initio calculations and bonded parameters

The *ab initio* calculations are used to identify the equilibrium geometry of the SeO_4^{2-} and SeO_3^{2-} ions, the corresponding force constant in Eqs. 5 and 6, and partial atomic charges of oxygen and selenium [16].

Density functional theory (DFT) is heavily rely on the choice of exchange-correlation functional. Even complex options do not guarantee accurate results [17]. Here we assess several GGA, hybrid, and double-hybrid DFT functionals, as well as the post-HF MP2 method, in their ability to describe vibrational properties of selenium oxyanions in aqueous solution. We use the def2-QZVPP basis set for the DFT and hybrid DFT calculations and the correlation-consistent cc-pVQZ with the auxiliary RI-C basis set for MP2 and double-hybrid DFT calculations.

However, explicit modeling of water in *ab initio* molecular dynamics at finite temperatures is still a challenging task. Even meta-GGA and hybrid-GGA functionals could not accurately reproduce the density of liquid water [18]. To avoid computationally expensive simulations of bulk water, we employ ionic structure optimization with the implicit Universal Solvation Model (SMD) [19, 20] and the Grimme dispersion correction D3BJ [21, 22]. The ORCA software package is used for the *ab initio* calculations [23, 24].

We perform the calculations in two steps. Firstly, the geometry of the ion is optimized by minimizing the system potential energy. Then, the Hessian matrix and vibrational frequencies are calculated in the harmonic approximation. The intramolecular values obtained for the Se–O distances, O–Se–O angles, and the frequency of the bond stretching mode ν_1 [25, 26] are compared with known experimental and theoretical data. We apply a modified Seminario method to obtain the intramolecular force field from the Hessian [27, 28] using the Sobtop program [29] .

2.3. Optimization of the non-bonded force field parameters and classical MD calculations

We use the hydration energies and as a criterion for the optimization of the force field [16]. We also calculate the effective ionic radii and their mobility in water as an independent check of the force field quality [30].

Classical molecular dynamics calculations have been performed in the GROMACS package [31]. We create initial configurations by placing one ion (SeO_4^{2-} or SeO_3^{2-}) in a cubic simulation cell with the 5 nm edge and then adding SPC/E water molecules to it [15]. This box approximately contains 4050 water molecules.

The calculations are performed at constant pressure and temperature (NPT ensemble). The pressure is maintained at 1 atm using a Parrinello-Rahman scheme with a time constant of 1.0 ps [32, 33]. The Nosé-Hoover thermostat is used to keep the temperature at 298 K [34]. Periodic boundary conditions are applied in three directions in the simulation. Ewald scheme is used to describe the electrostatic interactions between atoms [35]. The switch function between 1.0 and 1.2 nm is used to smoothly cut the L-J potential. To accelerate the optimization process, the length of the intermediate trajectories is set to 100 ps. The final set of parameters is analyzed from longer 1 ns runs. We use the 2 fs timestep in all calculations.

Radial distribution functions $g(r)$ are calculated with the same MD protocol, but the edge of the unit cell is equal to 3 nm, which approximately corresponds to 880 water molecules.

The mobility of the ions is estimated through the diffusion coefficients and mean square displacement calculations for the obtained force field. The simulation protocol is mostly identical to the calculation of $g(r)$, but the final trajectory run is 150 ns. In addition, several ionic concentrations are studied to overcome finite-size effects [36]. Calculation details are discussed further. The TRAVIS [37, 38] code is used to analyze the structural properties and mobility of the ions in this study.

2.4. Hydration energy calculations

We define the free energy of hydration ΔG_{hydr} as the sum of the work required to grow the cavity in the bulk solvent and then to charge the ion [39].

To determine its value, we apply Bennett's Acceptance Ratio (BAR) method, implemented in the GROMACS package [40]. The method allows determining the difference in free energy between two neighboring intermediate states, as previously shown in the literature [41]. In computer simulations, the change in the free energy of the process can be studied by changing the Hamiltonian of the system, which is a function of the control variable λ. The variable is used to turn off certain interactions in the

2

system in separate simulations. In this case, a significant overlap of the phase space sampling in the simulations is necessary to obtain the free energy difference. If the total free energy change is large, the overlap between a non-interacting state ($\lambda = 0$) and a fully interacting state ($\lambda = 1$) is extremely unlikely. Phase space overlap can be achieved by running simulations for a number of artificial states with intermediate values of λ along the chosen path [39]. The GROMACS software package supports a native way of specifying the control variable in the calculations.

The free energy change in the simulation ΔG_{sim} is defined as follows:

$$\Delta G_{sim} = \Delta G_{LJ} + \Delta G_{Coul}, \tag{7}$$

where the terms are the respective contributions from the interactions described by the Lennard-Jones and Coulomb potentials. They are expressed from the previously described procedure in the following form [39]:

$$\Delta G_{LJ} = \sum_{i=1}^{n_{LJ}-1} \Delta G_{LJ}^{BAR}(\lambda_i \longrightarrow \lambda_{i+1}) \tag{8}$$

$$\Delta G_{Coul} = \sum_{i=1}^{n_{Coul}-1} \Delta G_{Coul}^{BAR}(\lambda_i \longrightarrow \lambda_{i+1}) \tag{9}$$

The variables n_{LJ} and n_{Coul} in equations 8 and 9 are the number of intermediate states corresponding to cavity growth and charge insertion, respectively. The number of λ_i should be large enough to ensure sufficient phase space overlap in the calculations. However, increasing this number also slows down the optimization cycle. Combining these factors, we set n_{LJ} and n_{Coul} to 21 in this study, so the step of the control variables for the Lennard-Jones and Coulomb potentials is $\Delta\lambda = 0.05$.

For each value λ, we perform the modeling protocol described in Section 2.3. After that, we apply the Bennett acceptance factor method to obtain values of ΔG_{LJ} and ΔG_{Coul}.

Several correction terms are also added to the calculated hydration free energy:

$$\Delta G_{hydr} = \Delta G_{sim} + \Delta G_{press} + \Delta G_{surf} + \Delta G_{fs}. \tag{10}$$

These include a pressure correction ΔG_{press}, a surface dipole correction ΔG_{surf}, and a correction for finite-dimensional effects ΔG_{fs}. More details are provided in Ref. [39]. We use the previously calculated values $\Delta G_{press} = 7.92$ kJ/mol and $\Delta G_{surf} = -106.12$ kJ/mol [39]. We determine the value of ΔG_{fs} from the Hünenberger correction for the spherical ions, as described in the literature [42, 39].

2.5. Crystals structure modeling

To test the transferability of the created force field, we also use classical MD to model various solid selenate and selenite phases. The initial atomic positions are based on the experimental data, except for some selenite crystals, where the corresponding crystal structure is unknown. In that case, we used the sulfate crystal data as a reference. Unit cells are repeated in all directions to create the supercell with an edge of at least 5.2 nm.

The ClayFF force field [14] is used to describe the potential energy of the crystals. ClayFF has already proven itself as powerful tools for studying various clay and cement materials together with the SPC/E water [14]. We should note that our fitting protocol includes the rigid SPC/E model, while ClayFF assumes flexible water molecules. We presume that the structural properties of crystals are slightly affected by this difference, so we use flexible water for this part of the paper. The interaction parameters of the Lennard-Jones potential between different atomic types are obtained using a combination of arithmetic and geometric (Lorentz-Berthelot) combining rules [14]. MD calculations of crystal structures are performed in the LAMMPS package [43] for 0.5 ns in the NPT ensemble without any symmetry constraints imposed on the system, and all crystal cell parameters are allowed to vary. The timestep for the integration of the equations of motion was set to 1.0 fs. All calculations are performed under ambient conditions.

3. Results and Discussion

3.1. Ab initio modeling

We test several MP2 and DFT models, as in general more complexity does not lead to more accuracy. Assuming a close efficiency of the models for both selenate and selenite ions, a comparison of different *ab initio* approaches is performed only for the SeO_4^{2-} ion.

Although all tested DFT functionals successfully represent the tetrahedral geometry of SeO_4^{2-}, simple GGA PBE and BLYP functionals with D3BJ correction overestimate the equilibrium bond lengths and underestimate the vibrational frequency ν_1. The hybrid PBE0 + D3BJ DFT and MP2 + D3BJ models accurately reproduce previously reported bond lengths [44, 45, 46], although MP2 predicts a slightly larger value ν_1 (875 cm^{-1}). We take the equilibrium PBE0 + D3BJ geometry for further calculations with the double-hybrid DSD-PBEP86 and DSD-BLYP functionals, which are considered among the most robust and reliable models [47]. However, the difference in ν_1 values between the hybrid and double-hybrid models is about 1 cm^{-1}, which is much less than the unaccounted anharmonic effects. We select the DSD-PBEP86-D3BJ model for further studies, as the computational overhead is quite low. The equilibrium parameters for this model among the data from the literature are presented in Tables 1 and 2 for SeO_4^{2-} and SeO_3^{2-} respectively. Since the ions have symmetrical structures, only the averaged angle and bond values are shown.

As can be seen from Table 2, similar accuracy is observed for SeO_3^{2-}. Again, the vibrational frequency is

3

Table 1: Comparison of structural and vibrational properties of SeO_4^{2-}.

Source	Se−O, nm	O−Se−O, °	ν_1, cm^{-1}
DSD-PBEP86	0.1639	109.47	860
QMCF [45]	0.1640	109.0 ±10.0	812
BLYP [48]	0.165	109.42	856
Raman [49]	–	–	837
Raman [50]	–	–	835
Neutron scattering [44]	0.1640	110.0 ±3.0	836
LAXS [46]	0.1657	–	–
EXAFS [46]	0.1643	–	–

larger than the experimental value due to the unaccounted anharmonic effects [46, 51, 52, 53, 54].

Table 2: Comparison of the structural and vibrational properties of SeO_3^{2-}.

Source	Se−O, nm	O−Se−O, °	ν_1, cm^{-1}
DSD-PBEP86	0.1680	103.39	833
M05-2X [53]	0.1687	106.5	–
PBE0 [53]	0.1689	106.8	–
FC-MP [53]	0.1708	107.3	–
HF/ECP [53]	0.1662	106.4	–
HF/all-el. [51]	0.1664	106.4	–
HF [52]	0.1662	106.8	–
FC-MP2 [52]	0.1708	107.3	–
CISD+Q [52]	0.1699	107.1	–
MP2 [54]	–	–	771
LAXS [46]	0.1709	–	–
EXAFS [46]	0.1701	–	–
IR [54]	–	–	807
Raman [54]	–	–	807

We also calculate solvation energies, which are further used to fit the non-bonded parameters of the force field. For SeO_4^{2-}, our calculations provide the value of −1000 kJ/mol, while the experimental value is higher (−900 kJ/mol). However, all previously calculated energies are lower than the experimental data, the values of −1110 and −1047 kJ/mol were previously reported [55, 56, 57]. SeO_3^{2-} solvation energy is known only from the *ab initio* calculation. Wicke and Meleshyn [53] give the range between −939.7 and −1027.2 kJ/mol, while our value is lower (−1097 kJ/mol) due to the different solvation model. It should be noted that our reported hydration energies include the standard state correction 7.9 kJ/mol (change of a gas at 1 atm to a 1 M solution).

3.2. Evaluation of the force field parameters

The harmonic bond and angle terms (Eq. 5, 6) are obtained from the Hessian matrix with the modified Seminario method [28] in the Sobtop code [29] . The resulted parameters for SeO_4^{2-} and SeO_3^{2-} ions are given in Table 3.

Table 3: Harmonic bonds and angles force field parameters for selenium oxyanions

Ion	$i-j$	k_r, kJ/mol/nm^2	r_0, nm
SeO_4^{2-}	Se − O	3.247758×10^5	0.163923
SeO_3^{2-}	Se − O	2.874878×10^5	0.168000

Ion	$i-j-k$	k_θ, kJ/mol/rad^2	θ_0, °
SeO_4^{2-}	O − Se − O	627.316	109.47
SeO_3^{2-}	O − Se − O	904.765	103.39

Lennard-Jones and Couloumb parameters (Eq. 2, 3) are fitted to reproduce the hydration free energy ΔG_{hydr} and the effective ionic radius using the algorithm described in Ref. [39]. The target values are taken from the *ab initio* simulations, presented in Section 3.1. The effective radii from the LAXS experiments [46] are used as a control parameter, as these values are not available in the implicit solvent model.

We start the optimization process for the SeO_4^{2-} ion. The Mulliken atomic charges [58] from the *ab initio* calculations are used as an initial guess for the Coulomb potential (Eq. 2). The starting values for the Lennard-Jones parameters (Eq. 3) are deduced from the SO_4^{2-} constants ($\varepsilon_S = 0.837$ kJ/mol, $\sigma_S = 0.355$ nm, $\varepsilon_{O_S} = 0.650$ kJ/mol, $\sigma_{O_S} = 0.368$ nm) [59, 39], since the oxyanions of Se and S have similar properties [46].

The following parameters are chosen for optimization: ε_{Se}, σ_{Se}, $\sigma_{O_{Se}}$, $q_{O_{Se}}$. Since the total charge of the ion is −2, a change of $q_{O_{Se}}$ leads to a change of q_{Se}. We do not vary $\varepsilon_{O_{Se}}$ to reduce the number of adjustable parameters [39].

For simplicity, we consider these parameters independently. In this case, global optimization can be achieved by successive optimization of each value in order to minimize the difference between classical MD and *ab initio* hydration energy ΔG_{hydr}. Firstly, we optimize the selenium parameters σ_{Se} and ε_{Se} and then proceed to the oxygen parameter $\sigma_{O_{Se}}$. We choose an acceptable range for each variable and then use the multigrid search to find the best combination of the parameters. The fineness of the grid is adjusted after each successful optimization cycle. To accelerate the calculations, we use short 100 ps MD trajectory for each λ during optimization. This slightly increases the uncertainty of ΔG_{hydr}, but significantly speeds up the calculation. However, for the final set of parameters, we use longer 1 ns trajectories.

We could find the reasonable force field without tuning the initial atomic charges. However, they can be further adjusted to more accurately reproduce some other properties.

The above procedure for SeO_4^{2-} ion is also performed for SeO_3^{2-}, but with a slight modification of the initial guess. We take the already found Lennard-Jones parameters ε_{Se}, σ_{Se} without further optimization and vary only the $\sigma_{O_{Se}}$ parameter.

The obtained parameters of the Lennard-Jones and

4

Coulomb potentials are shown in Table 4.

Table 4: Lennard-Jones and Coulomb potentials parameters for $SeO_4{}^{2-}$ and $SeO_3{}^{2-}$.

Ion	i	q_i, e	ε_i, kJ/mol	σ_i, nm
$SeO_4{}^{2-}$	Se	1.4084	0.76	0.455
	O	-0.8521	0.65	0.340
$SeO_3{}^{2-}$	Se	1.0846	0.76	0.455
	O	-1.0282	0.65	0.373

Given the existence of multiple independent parameters within the optimization system, it can be reasonably assumed that a similar result can be achieved with a different set of parameters. Nevertheless, the obtained force field demonstrates good transferability, as will be discussed further.

Table 5 presents the results of the calculation of the hydration free energy by the classical MD for selenium oxyanions, as well as their comparison with the literature data. The selected L-J and Coulomb parameters demonstrate a very good agreement with the *ab initio* calculations. In the case of $SeO_4{}^{2-}$ ion, our force field gives $\Delta G_{hydr} = -1001.3 \, \mathrm{kJ/mol}$, while the target *ab initio* value is $-1000.05 \, \mathrm{kJ/mol}$.

Similar accuracy is observed for the $SeO_3{}^{2-}$ ion. The classical MD gives $\Delta G_{hydr} = -1096.13$ kJ/mol, while our *ab initio* modeling predicts $\Delta G_{hydr} = -1097.64$ kJ/mol.

3.3. Structural properties of the hydrated oxyanions

Table 6 presents the average bond lengths for the $SeO_4{}^{2-}$ and $SeO_3{}^{2-}$ in water. The intramolecular pairs Se – O_{Se} as well as the intermolecular Se – O_w, Se – H_w, O_{Se} – O_w and O_{Se} – H_w are studied. The effective radius is also calculated for the observed ions. It is usually defined as the average distance between the center of mass of the anion and the oxygen atoms of surrounding water molecules, i.e., $r(Se – O_w)$ [39]. However, hydration spheres are not included in the experimental values. Therefore, the experimental radius of the water (0.140 nm) is subtracted from this distance [60] to obtain the effective radius.

Considering $SeO_4{}^{2-}$ ions, the Se – O_{Se} bond length is 0.164 nm, the value between 0.164 and 0.166 nm is observed in the experiments. The effective radius of $SeO_4{}^{2-}$ is 0.257 nm, which is close to the experimental value of 0.249 nm [46]. Moreover, the Se – O_w distance is 0.397 nm, which is in agreement with both the LAXS data [46] and the results of QMCF modeling [45]. The average interatomic distances between O_{Se} and water oxygen is 0.285 nm and 0.189 nm between O_{Se} and water hydrogen.

The reported values are taken from the correlation functions $g(r)$ and running coordination number $CN(r)$ presented for the selenate-containing system in Figure 1. These functions illustrate the structure of the solvation shell. We determine the position of the second peaks in Figure 1, which is located at a distance of approximately 0.6 nm for the Se – O_w pair and approximately 0.45 nm

for the Se – H_w pair. A plateau at 0.45 – 0.5 nm can be noticed for the O_{Se} – O_w pair. Its origin may be due to the influence of other O_{Se} atoms. For the O_{Se} – H_w pair , the intensities of the second and third peaks are close, which reflects the rotation of water molecules near the solvation shell. By evaluating the number of neighbors through the coordination number function, we find that the average number of water molecules in the first solvation sphere is 14.22. This value is close to the value for $SO_4{}^{2-}$ from Ref. [39].

A similar analysis is also performed for the selenite ion. The average interatomic distances between the nearest atoms in the solvation sphere for this ion are also summarized in Table 6. The length of the intramolecular bond between selenium and oxygen, obtained by classical MD calculations, is equal to 0.169 nm, which is greater than the same bond in the $SeO_4{}^{2-}$ ion. This value is in good agreement with the data in the literature, where it varies between 0.1687 to 0.171 nm [53, 46, 61]. The interatomic distance between selenium and water oxygen is 0.393 nm, slightly exceeding previously reported values 0.375 – 0.387 nm in Refs. [53] and [46]. However, we correctly reproduce that selenite Se−O_w distance is smaller than the selenate value [46, 45]. Additionally, the estimated effective radius of $SeO_3{}^{2-}$ is 0.253 nm versus 0.239 nm in the experiment [46].

The plots of the radial distribution and coordination functions for the selenite-containing system are shown in Figure 2. We note the appearance of a small shoulder in the vicinity of 0.45 nm for the Se – O_w pair, which correlates with the experimental observations of clustered water molecules outside the lone electron pair on selenium [46]. This effect can also be observed on the Se–H_w plot, where the second and third peaks are somewhat merged into a double peak.

3.4. Anionic mobility

The force field should reproduce the mobility of a particle with sufficient accuracy. We calculate the diffusion coefficients using the Einstein's ratio [62]:

$$D = \frac{1}{6} \lim_{t \longrightarrow \infty} \frac{dMSD(r)}{dt}, \tag{11}$$

where MSD is the mean square displacement of an ion.

We employ the additional 100 ns MD run in the NVT ensemble to calculate the time-averaged mean square displacements. Atomic positions are dumped every 500 steps. To calculate the tracer diffusion coefficient, we use the TRAVIS package [37, 38]. We observe that even long 100 ns MD trajectories do not allow us to obtain the reproducible result in a series of independent runs. As a compromise, we set the correlation depth at 25 ps to avoid fitting over less accurate long-time correlations [39].

As diffusion coefficients are sensitive to finite-size effects due to long-range nature of hydrodynamic and electrostatic forces [63], we perform several calculations with different cell sizes ($L = 3, 4, 5, 6$ nm) to obtain D_L at each
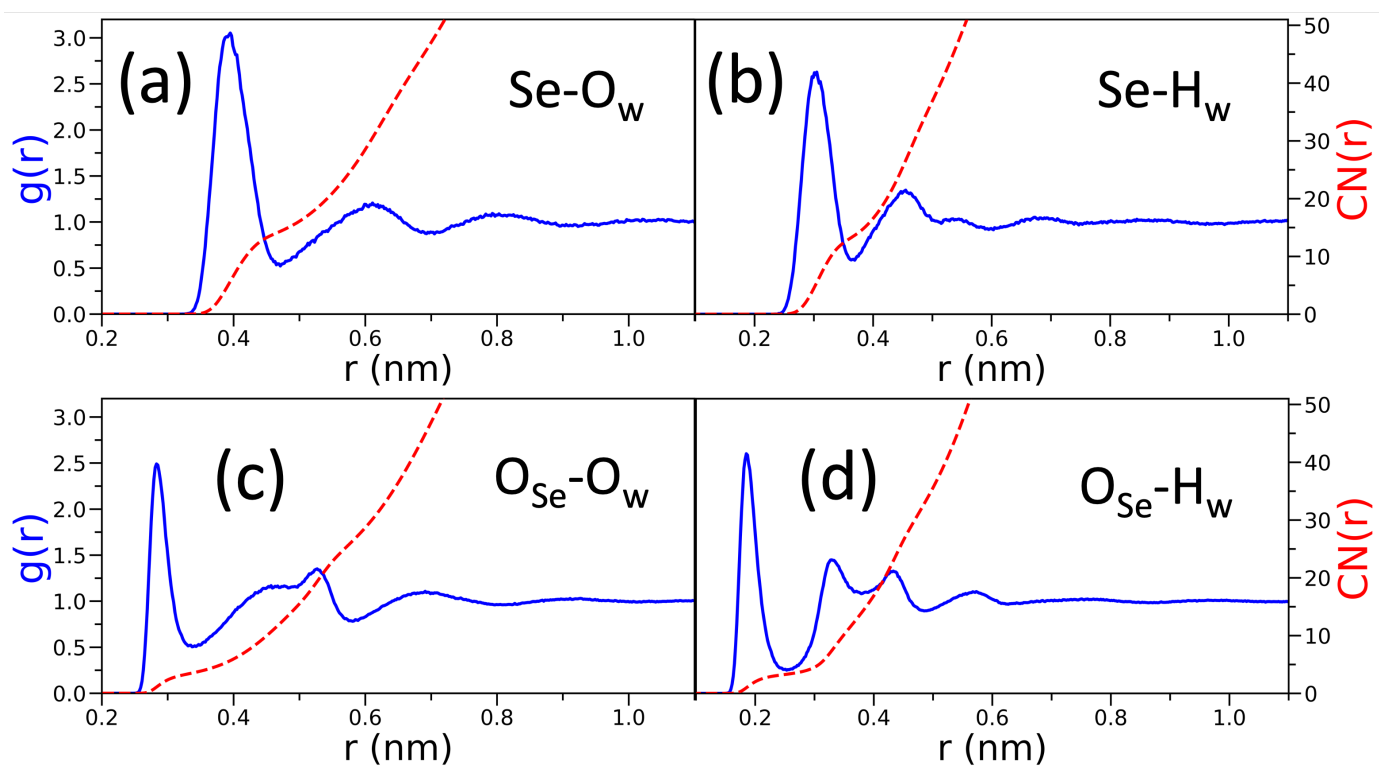
5

Figure 1: Radial distribution functions and their number integrals for SeO_4^{2-} oxyanions.
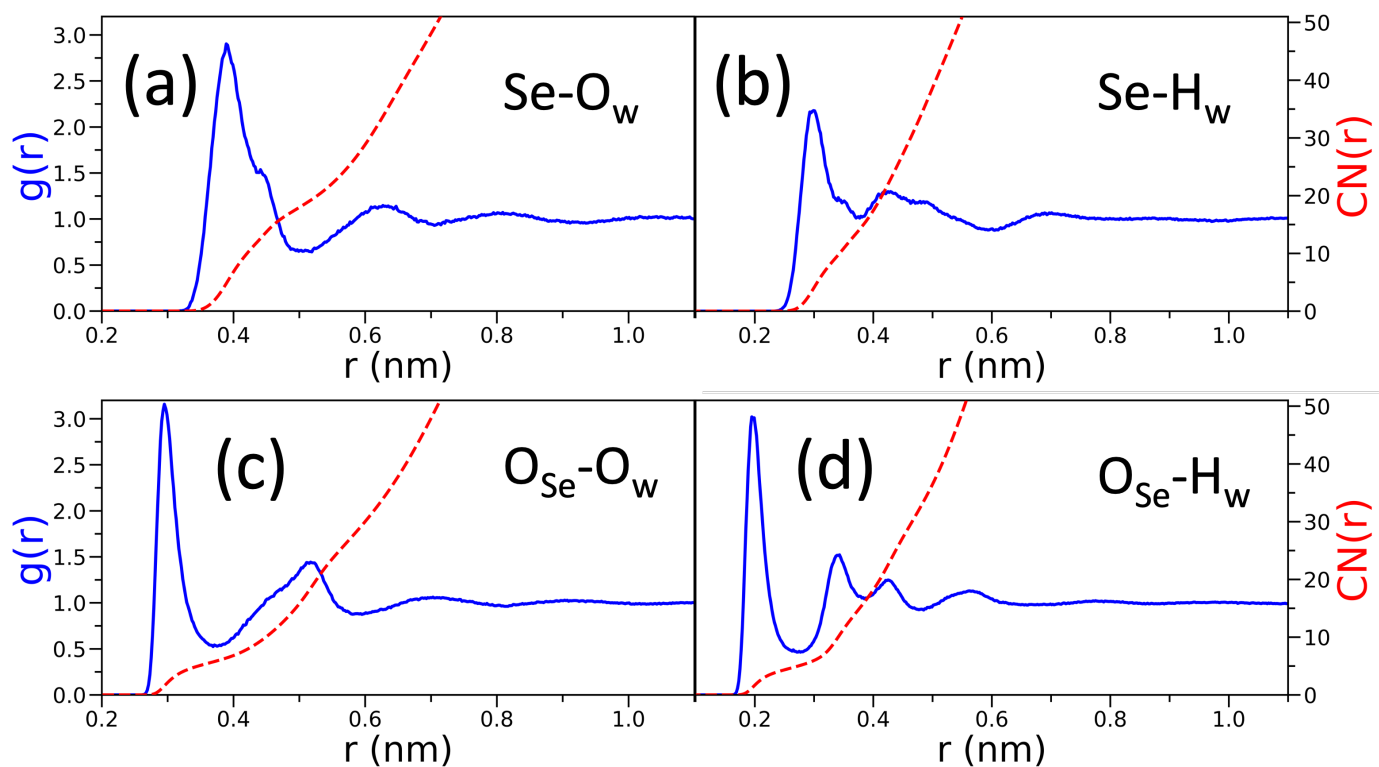

Figure 2: Radial distribution functions and their number integrals for SeO_3^{2-} oxyanions.

6

Table 5: Results of the hydration free energy calculation with the classical MD. All values are given in kJ/mol.

Ion	ΔG_{LJ}	ΔG_{Coul}	ΔG_{press}	ΔG_{surf}	ΔG_{fs}	ΔG_{hydr}	Source
SeO_4^{2-}	1.62	−1117.34	7.92	106.1	0.60	−1001.10	MD, this work
	–	–	–	–	–	−1000.1	double-hybrid DFT, this work
	–	–	–	–	–	−900	Experimental [55, 56]
	–	–	–	–	–	−1110	Thermodynamics [55, 56]
	–	–	–	–	–	−1047	Cosmo RS [57]
SeO_3^{2-}	6.90	−1217.63	7.92	106.1	0.58	−1096.13	MD, this work
	–	–	–	–	–	−1097.64	double-hybrid DFT, this work
	–	–	–	–	–	−939.7 to −1027.2	hybrid DFT & MP2 [53]

Table 6: Average interatomic distances in hydrated selenium oxyanions: MD modeling and literature data. All values are given in nm.

Ion	$Se - O_{Se}$	$Se - O_w$	$Se - H_w$	$O_{Se} - O_w$	$O_{Se} - H_w$	Source
SeO_4^{2-}	0.164	0.397	0.307	0.285	0.189	MD, this work
	0.1657	0.394	–	–	–	LAXS [46]
	0.1643	–	–	–	–	EXAFS [46]
	0.164	–	–	–	–	Neutron scattering [44]
	0.164	0.400	–	–	–	QMCF-MD [45]
	0.165	–	–	0.275	0.178	DFT [48]
SeO_3^{2-}	0.169	0.393	0.301	0.296	0.199	MD, this work
	0.171	0.387	–	–	–	LAXS [46]
	0.170	–	–	–	–	EXAFS [46]
	0.1687	0.375	–	–	0.183, 0.185	Hybrid-DFT [53]
	0.169	–	–	0.275	0.175	DFT [61]

cell size, so we can extrapolate results to the infinite cell and get D_∞ [36].

The system with one ion surrounded by water molecules is not charge-neutral. As electrostatic effects could affect the diffusivity, we have tested the validity of method by calculating the well-known diffusion coefficients of SPC/E water. The calculated self-diffusion coefficient of water $D_{H_2O_\infty} = 2.35 \pm 0.01$ m^2/s, which is close to the literature data [64, 65, 66]. However, some authors report higher values [39, 67], which is most likely due to the different MD protocol.

The calculated diffusion coefficients for oxyanions are presented in Table 7. The calculated self-diffusion coefficient of the SPC/E water model is larger than the experimental value, and some authors additionally scale the tracer diffusion coefficient in the SPC/E water by a factor of 0.82 [39]. For clarity, we show the diffusion coefficients with and without correction in Table 7.

The tracer diffusion coefficients are close to the experimental data. Thus, for SeO_4^{2-} it is 0.8×10^{-9} m^2/s, and for SeO_3^{2-} it is 0.85×10^{-9} m^2/s. Taking into account three independent runs, the calculated uncertainty is about 0.25×10^{-9} m^2/s. Since the force field parameters are not fitted to this property, we could approve the predictive power of the generated force field.

3.5. Solid selenate phases

As mentioned above, sulfate anions could be replaced with SeO_4^{2-} in crystalline calcium sulfoaluminate hy-
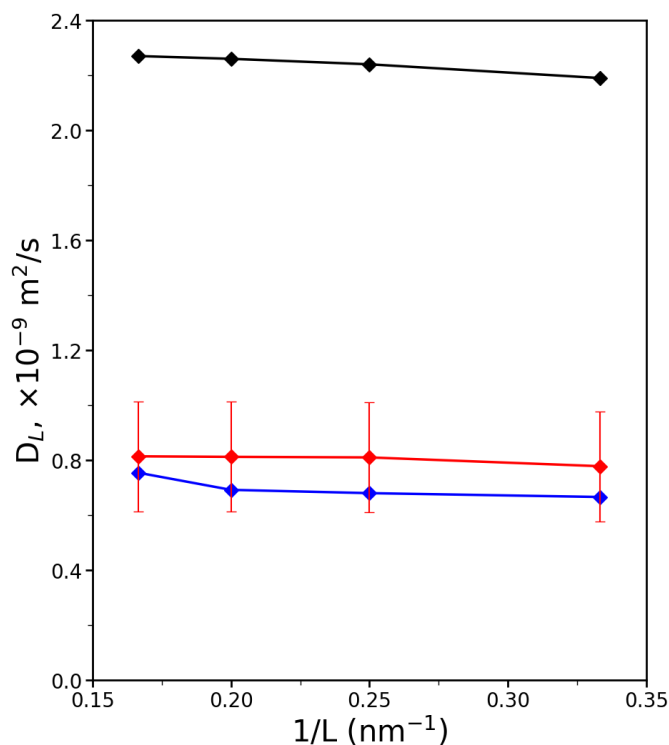

Figure 3: Diffusion coefficients dependence from the cell size. The color pallete is as follows: red is SeO_3^{2-}, blue is SeO_4^{2-}, black is for H_2O. Measurement uncertainty for ions is shown only for SeO_3^{2-} for clarity.

7

Table 7: Diffusion coefficients of SeO_4^{2-} and SeO_3^{2-} in water.

Ion	$D \times 10^9$, m^2/s
SeO_4^{2-}	0.80
	0.98*
	0.714 [68]
	0.94 [69]
SeO_3^{2-}	0.85
	1.10*
	0.89 [70]

*SPC/E model self-diffusion scaling

drates (AFt and AFm phases) [6, 7, 8, 9]. Thus, the SeO_4-AFt and SeO_4-AFm phases are stable in the cement matrix. In addition, calcium selenate phases can precipitate in the presence of calcium cations, selanate anions and water molecules in the pores of hardened cement, where the typical pH values are about 12–13. The $CaSeO_4 \cdot 2H_2O$ compound [71] similar to gypsum and $CaSeO_4 \cdot 0.625H_2O$ phase [72] similar to bassanite are known.

Using the new parameterization for SeO_4^{2-} in conjuction with the ClayFF force field, we model the following hydrated selenate phases: $CaSeO_4 \cdot 2H_2O$, $CaSeO_4 \cdot 0.625H_2O$, SeO_4-AFt phase ($3CaO \cdot Al_2O_3 \cdot 3CaSeO_4 \cdot 30H_2O$) and SeO_4-AFm phase ($3CaO \cdot Al_2O_3 \cdot CaSeO_4 \cdot 14H_2O$). The atomic structures of the calcium selenate phases are adopted from the experimental data [71, 72], while SeO_4-AFt and SeO_4-AFm structures are based on SO_4-AFt (ettringite) and SO_4-AFm (monosulfoaluminate) phases [73, 74] with the additional water in the interlayer to match the above chemical formulas. The calculated crystallographic parameters are listed in Table 8. All crystals remain stable during the simulation. However, the a and c lattice parameters of $CaSeO_4 \cdot 2H_2O$ structure significantly differ from the experimental values [71] (up to 18%). This discrepancy is probably related to the ClayFF model, as a similar error is known for the equivalent structure of gypsum ($CaSO_4 \cdot 2H_2O$) [75]. Apparently, additional detailed parameterization for the $CaSeO_4 \cdot 2H_2O$ model is required, as it is done for the gypsum with the IFF force field [76].

Surprisingly, the $CaSeO_4 \cdot 0.625H_2O$ model shows a good agreement with the experimental data [72]. The deviation in the calculated lattice parameters is less than 5%. The SeO_4-ettringite model shows slightly larger deviation (up to 5%) from the X-ray data [9]. For the SeO_4-AFm phase model it is only possible to compare the layer distance, which is slightly smaller than the experimental value [6].

4. Conclusion

In this work, we propose the force fields to model selenate and selenite ions in aqueous solutions using classical molecular dynamics. The corresponding parameters are summarized in Tables 3 and 4. In addition, we provide these parameters in the GROMACS format as a Supplementary Material. The non-bonded terms of the force fields are fitted to reproduce the *ab initio* geometries and harmonic vibrations of ions with the implicit solvation model. Lennard-Jones and Coulomb terms are adjusted to match the *ab initio* solvation free energies. Although we developed our model in conjunction with the SPC/E water, it can be extended for other popular non-polarizable three- or four-point water models.

We verify the created force field by calculating tracer diffusion coefficients and structural parameters of some solid hydrated selenate phases. Both new selenite (SeO_3^{2-}) and selenate (SeO_4^{2-}) force fields can be used to study the inner- and outer-sphere complexes on the surfaces of clay, cement, and other materials using classical molecular simulations (e.g., ClayFF and IFF force fields [14, 77]). Furthermore, selenate (SeO_4^{2-}) force field can be used for modelling hydrated layered and nanoporous minerals.

Acknowledgments

References

[1] B. Grambow, Mobile fission and activation products in nuclear waste disposal, Journal of Contaminant Hydrology 102 (2008) 180–186. doi:10.1016/j.jconhyd.2008.10.006.

[2] V. Krupskaya, D. Biryukov, P. Belousov, V. Lekhov, A. Romanchuk, S. Kalmykov, Use of natural clay materials to increase nuclear and radiation safety of nuclear legacy facilities, Radioactive Waste 2 (3) (2018) 30–43.

[3] E. Abramova, N. Popova, G. Artemiev, K. Boldyrev, K. Kazakov, D. Kryuchkov, A. Safonov, Biological factors affecting the evolution of safety barrier materials in the yeniseisky deep geological repository, Engineering Geology 312 (2023) 106931. doi:10.1016/j.enggeo.2022.106931.

[4] O. Ilina, V. Krupskaya, S. Vinokurov, S. Kalmykov, State-of-art in the development and use of clay materials as engineered safety barriers at radioactive waste conservation and disposal facilities in russia, Radioactive Waste 4 (9) (2019) 71–84. doi:10.25283/2587-9707-2019-4-71-84.

[5] B. Grambow, M. Lopez-Garcia, J. Olmeda, M. Grive, N. Marty, S. Grangeon, F. Claret, S. Lange, G. Deissmann, M. Klinkenberg, D. Bosbach, C. Bucur, I. Florea, R. Dobrin, M. Isaacs, D. Read, J. Kittnerova, B. Drtinova, D. Vopalka, N. Cevirim-Papaioannou, N. Ait-Mouheb, X. Gaona, M. Altmaier, L. Nedyalkova, B. Lothenbach, J. Tits, C. Landesman, S. Rasamimanana, S. Ribet, Retention and diffusion of radioactive and toxic species on cementitious systems: Main outcome of the CEBAMA project., Applied Geochemistry 112 (2020) 104480.

[6] I. Baur, C. Johnson, The solubility of selenate-AFt ($3CaO \cdot Al_2O_3 \cdot 3CaSeO_4 \cdot 37.5H_2O$) and selenate-AFm ($3CaO \cdot Al_2O_3 \cdot CaSeO_4 \cdot xH_2O$), Cement and Concrete Research 33 (11) (2003) 1741–1748. doi:10.1016/S0008-8846(03)00151-0.

[7] B. Guo, K. Sasaki, T. Hirajima, Selenite and selenate uptaken in ettringite: Immobilization mechanisms, coordination chemistry, and insights from structure, Cement and Concrete Research 100 (2017) 166–175. doi:10.1016/j.cemconres.2017.07.004.

8

Table 8: Unit cell parameters of some solid selenate phases

Structure	a, Å	b, Å	c, Å	α, °	β, °	γ, °
$CaSeO_4 \cdot 2H_2O^*$	6.8450	15.3678	5.7334	90.0	111.2	90.0
$CaSeO_4 \cdot 2H_2O$ [71]	5.8377	15.5212	6.5951	90	116.837	120
$CaSeO_4 \cdot 0.625H_2O^*$	14.8617	14.8344	13.7782	90.2	89.9	118.6
$CaSeO_4 \cdot 0.625H_2O$ [72]	14.1683	14.1683	13.4241	90	90	120
SeO_4-ettringite*	11.8827	11.8961	21.8216	90.2	89.9	119.9
SeO_4-ettringite [9]	11.387	11.387	21.46	90	90	120
SeO_4-AFm*	5.796	5.789	9.817**	88.7	91.0	119.4
SeO_4-AFm [6]	—	—	10.2**	—	—	—

* – this work; **– layer distance.

[8] S. Grangeon, N. Marty, N. Maubec, F. Warmont, F. Claret, Selenate sorption by hydrated calcium aluminate (AFm): Evidence for sorption reversibility and implication for the modeling of anion retention, ACS Earth and Space Chemistry 4 (2) (2020) 229–240. doi:10.1021/acsearthspacechem.9b00286.

[9] D. Hassett, G. McCarthy, P. Kumarathasan, D. Pflughoeft-Hassett, Synthesis and characterization of selenate and sulfate–selenate ettringite structure phases, Materials Research Bulletin 21 (11) (1990) 1347–1354. doi:10.1016/0025-5408(90)90216-O.

[10] R. Mishra, A. Mohamed, D. Geissbühler, H. Manzano, T. Jamil, R. Shahsavari, A. Kalinichev, S. Galmarini, L. Tao, H. Heinz, R. Pellenq, A. van Duin, S. Parker, R. Flatt, P. Bowen, cemff: A force field database for cementitious materials including validations, applications and opportunities, Cement and Concrete Research 102 (2017) 68–89. doi:10.1016/j.cemconres.2017.09.003.

[11] X. Liu, C. Tournassat, S. Grangeon, A. Kalinichev, Y. Takahashi, M. Fernandes, Molecular-level understanding of metal ion retention in clay-rich materials, Nature Reviews: Earth & Environment 3 (2022) 461–476. doi:10.1038/s43017-022-00301-z.

[12] P. Yang, N. Rampal, J. Weber, J. Bracco, P. Fenter, A. G. Stack, S. Lee, Synergistic enhancement of lead and selenate uptake at the barite (001)–water interface, Environmental Science & Technology 56 (23) (2022) 16801–16810. doi:10.1021/acs.est.2c04413.

[13] R. Cygan, J.-J. Liang, A. Kalinichev, Molecular models of hydroxide, oxyhydroxide, and clay phases and the development of a general force field, The Journal of Physical Chemistry B 108 (4) (2004) 1255–1266. doi:10.1021/jp0363287.

[14] R. Cygan, J. Greathouse, A. Kalinichev, Advances in clayff molecular simulation of layered and nanoporous materials and their aqueous interfaces, The Journal of Physical Chemistry C 125 (32) (2021) 17573–17589. doi:10.1021/acs.jpcc.1c04600.

[15] H. Berendsen, J. Grigera, T. Straatsma, The missing term in effective pair potentials, The Journal of Physical Chemistry 91 (24) (1987) 6269–6271. doi:10.1021/j100308a038.

[16] D. Horinek, S. Mamatkulov, R. Netz, Rational design of ion force fields based on thermodynamic solvation properties, The Journal of Chemical Physics 130 (12) (2009) 124507. doi:10.1063/1.3081142.

[17] M. Medvedev, I. Bushmarinov, J. Sun, J. Perdew, K. Lyssenko, Density functional theory is straying from the path toward the exact functional, Science 355 (6320) (2017) 49–52. doi:10.1126/science.aah5975.

[18] C. Zhang, F. Tang, M. Chen, J. Xu, L. Zhang, D. Qiu, J. Perdew, M. Klein, X. Wu, Modeling liquid water by climbing up jacob's ladder in density functional theory facilitated by using deep neural network potentials, Journal of Physical Chemistry B 125 (2021) 11444–11456. doi:10.1021/acs.jpcb.1c03884.

[19] V. Barone, M. Cossi, Quantum calculation of molecular energies and energy gradients in solution by a conductor solvent model, The Journal of Physical Chemistry A 102 (11) (1998) 1995–2001. doi:10.1021/jp9716997.

[20] A. Marenich, C. Cramer, D. Truhlar, Universal solvation model based on solute electron density and on a continuum model of the solvent defined by the bulk dielectric constant and atomic surface tensions, The Journal of Physical Chemistry B 113 (18) (2009) 6378–6396. doi:10.1021/jp810292n.

[21] S. Grimme, S. Ehrlich, L. Goerigk, Effect of the damping function in dispersion corrected density functional theory, Journal of Computational Chemistry 32 (7) (2011) 1456–1465. doi:10.1002/jcc.21759.

[22] J. Tomasi, B. Menucci, R. Cammi, Quantum mechanical continuum solvation models, Chemical Reviews 105 (8) (2005) 2999–3094. doi:10.1021/cr9904009.

[23] F. Neese, The ORCA program system, WIREs Computational Molecular Science 2 (1) (2012) 73–78. doi:10.1002/wcms.81.

[24] F. Neese, F. Wennmohs, U. Becker, C. Riplinger, The ORCA quantum chemistry program package, The Journal of Chemical Physics 152 (22) (2020) 224108. doi:10.1063/5.0004608.

[25] M. Volkenshtein, L. Gribov, M. Eliashevich, B. Stepanov, Vibrations of molecules (in Russian), Nauka, 1972.

[26] H. Schulze, N. Weinstock, A. Müller, G. Vandrish, Raman intensities and force constants of PO_4^{3-}, SO_4^{2-}, ClO_4^-, SeO_4^{2-} and BrO_4^-, Spectrochimica Acta Part A: Molecular Spectroscopy 29 (9) (1973) 1705–1709. doi:10.1016/0584-8539(73)80122-9.

[27] J. Seminario, Calculation of intramolecular force fields from second-derivative tensors, International Journal of Quantum Chemistry 60 (7) (1996) 1271–1277. doi:10.1002/(SICI)1097-461X(1996)60:7<1271::AID-QUA8>3.0.CO;2-W.

[28] A. Allen, M. Payne, D. Cole, Harmonic force constants for molecular mechanics force fields via hessian matrix projection, Journal of Chemical Theory and Computation 14 (1) (2018) 274–281. doi:10.1021/acs.jctc.7b00785.

[29] T. Lu, Sobtop, version 1.0(dev3.1), http://sobereva.com/soft/Sobtop.

[30] M. Orekhov, Effect of divalent ion coordination on ion diffusion in organic liquids, Journal of Molecular Liquids 343 (2021) 117647. doi:10.1016/j.molliq.2021.117647.

[31] S. Pronk, S. Páll, R. Schulz, P. Larsson, P. Bjelkmar, R. Apostolov, M. Shirts, J. Smith, P. Kasson, D. van der Spoel, B. Hess, E. Lindahl, GROMACS 4.5: a high-throughput and highly parallel open source molecular simulation toolkit, Bioinformatics 29 (7) (2013) 845–854. doi:10.1093/bioinformatics/btt055.

[32] M. Parrinello, A. Rahman, Crystal structure and pair potentials: A molecular-dynamics study, Physical Review Letters 45 (1980) 1196–1199. doi:10.1103/PhysRevLett.45.1196.

[33] M. Parrinello, A. Rahman, Polymorphic transitions in single crystals: A new molecular dynamics method, Journal of Applied Physics 52 (12) (1981) 7182–7190. doi:10.1063/1.328693.

[34] W. Hoover, Constant-pressure equations of motion, Physical Review A 34 (1986) 2499–2500. doi:10.1103/PhysRevA.34.2499.

[35] A. Toukmaji, J. Board, Ewald summation techniques in perspective: a survey, Computer Physics Communications 95 (2) (1996) 73–92. doi:10.1016/0010-4655(96)00016-1.

[36] M. Orekhov, Improving molecular dynamics calculation of diffusivity in liquids with theoretical models, Journal of Molecular Liquids 322 (2021) 114554. doi:10.1016/j.molliq.2020.114554.

[37] M. Brehm, B. Kirchner, TRAVIS – a free analyzer and visualizer

9

for monte carlo and molecular dynamics trajectories, Journal of Chemical Information and Modeling 51 (8) (2011) 2007–2023. doi:10.1021/ci200217w.

[38] M. Brehm, M. Thomas, S. Gehrke, B. Kirchner, TRAVIS – a free analyzer for trajectories from molecular simulation, The Journal of Chemical Physics 152 (16) (2020) 164105. doi:10.1063/5.0005078.

[39] C. Williams, P. Carbone, A classical force field for tetrahedral oxyanions developed using hydration properties: The examples of pertechnetate (TcO_4^-) and sulfate (SO_4^{2-}), The Journal of Chemical Physics 143 (17) (2015) 174502. doi:10.1063/1.4934964.

[40] C. Bennett, Efficient estimation of free energy differences from Monte Carlo data, Journal of Computational Physics 22 (2) (1976) 245–268. doi:10.1016/0021-9991(76)90078-4.

[41] A. de Ruiter, S. Boresch, C. Oostenbrink, Comparison of thermodynamic integration and bennett acceptance ratio for calculating relative protein-ligand binding free energies, Journal of Computational Chemistry 34 (12) (2013) 1024–1034. doi:10.1002/jcc.23229.

[42] P. Hünenberger, J. A. McCammon, Ewald artifacts in computer simulations of ionic solvation and ion–ion interaction: A continuum electrostatics study, The Journal of Chemical Physics 110 (4) (1999) 1856–1872. doi:10.1063/1.477873.

[43] A. Thompson, H. M. Aktulga, R. Berger, D. Bolintineanu, W. Brown, P. Crozier, P. in 't Veld, A. Kohlmeyer, S. Moore, T. Nguyen, R. Shan, M. Stevens, J. Tranchida, C. Trott, S. Plimpton, LAMMPS - a flexible simulation tool for particle-based materials modeling at the atomic, meso, and continuum scales, Computer Physics Communications 271 (2022) 108171. doi:10.1016/j.cpc.2021.108171.

[44] M. Dammak, T. Mhiri, A. Cousson, Neutron structural and vibrational studies of dipotassium selenate tellurate, Journal of Alloys and Compounds 407 (1) (2006) 176–181. doi:10.1016/j.jallcom.2005.06.044.

[45] T. Sakwarathorn, S. Pongstabodee, V. Vchirawongkwin, L. Canaval, A. Tirler, T. Hofer, Characteristics of selenate in aqueous solution – an ab initio QMCF-MD study, Chemical Physics Letters 595-596 (2014) 226–229. doi:10.1016/j.cplett.2014.01.046.

[46] L. Eklund, I. Persson, Structure and hydrogen bonding of the hydrated selenite and selenate ions in aqueous solution, Dalton Transactions 43 (2014) 6315–6321. doi:10.1039/C3DT53468E.

[47] L. Goerigk, A. Hansen, C. Bauer, S. Ehrlich, A. Najibi, S. Grimme, A look at the density functional theory zoo with the advanced gmtkn55 database for general main group thermochemistry, kinetics and noncovalent interactions, Physical Chemistry Chemical Physics 19 (2017) 32184–32215. doi:10.1039/C7CP04913G.

[48] S. Borah, P. Kumar, Ab initio molecular dynamics investigation of structural, dynamic and spectroscopic aspects of Se(VI) species in the aqueous environment, Physical Chemistry Chemical Physics 18 (2016) 14561–14568. doi:10.1039/C6CP01835A.

[49] G. E. Walrafen, Raman Spectral Studies of Aqueous Solutions of Selenic Acid, The Journal of Chemical Physics 39 (6) (1963) 1479–1492. doi:10.1063/1.1734469.

[50] M. Gupta, L. Surendra, S. Kaushik, G. Jere, Solid-state effects on selenate vibrations in yttrium and some rare earth selenates, Journal of Solid State Chemistry 43 (3) (1982) 359–363. doi:10.1016/0022-4596(82)90253-5.

[51] V. Solomonik, A. Marenich, V. Sliznev, Ab initio studies on the structure and vibrational spectra of alkali-metal sulfites and selenites, Russian Journal of Coordination Chemistry 24 (1998) 457.

[52] A. Marenich, V. Solomonik, The structure and the vibrational spectra of XO_2 molecules and XO_3^{2-} ions (X = S, Se, and Te), Russian Journal of Physical Chemistry 73 (1999) 1993.

[53] H. Wicke, A. Meleshyn, Microhydration of the selenite dianion: A theoretical study of structures, hydration energies, and electronic stabilities of $SeO_3^{2-}(H_2O)_n$ ($n = 0 - 6, 9$) clusters, Journal of Physical Chemistry A 114 (2010) 8948–8960.

[54] J. Kretzschmar, N. Jordan, E. Brendler, S. Tsushima, C. Franzen, H. Foerstendorf, M. Stockmann, K. Heim, V. Brendler, Spectroscopic evidence for selenium(IV) dimerization in aqueous solution, Dalton Transactions 44 (2015) 10508–10515. doi:10.1039/C5DT00730E.

[55] Y. Marcus, A simple empirical model describing the thermodynamics of hydration of ions of widely varying charges, sizes, and shapes, Biophysical Chemistry 51 (2) (1994) 111–127. doi:10.1016/0301-4622(94)00051-4.

[56] Y. Marcus, Thermodynamics of solvation of ions. Part 5.—Gibbs free energy of hydration at 298.15 K, Journal of the Chemical Society, Faraday Transactions 87 (1991) 2995–2999. doi:10.1039/FT9918702995.

[57] M. Andersson, S. Stipp, Predicting hydration energies for multivalent ions, Journal of Computational Chemistry 35 (28) (2014) 2070–2075. doi:10.1002/jcc.23733.

[58] R. S. Mulliken, Electronic Population Analysis on LCAO–MO Molecular Wave Functions. I, The Journal of Chemical Physics 23 (10) (1955) 1833–1840. doi:10.1063/1.1740588.

[59] C. Williams, N. Burton, K. Travis, J. Harding, The development of a classical force field to determine the selectivity of an aqueous Fe^{3+}-EDA complex for TcO_4^- and SO_4^{2-}, Journal of Chemical Theory and Computation 10 (8) (2014) 3345–3353. doi:10.1021/ct500198c.

[60] R. Schmid, A. Miah, V. Sapunov, A new table of the thermodynamic quantities of ionic hydration: values and some applications (enthalpy–entropy compensation and born radii), Physical Chemistry Chemical Physics 2 (2000) 97–102. doi:10.1039/A907160A.

[61] S. Borah, P. Kumar, Ab initio molecular dynamics study of Se(IV) species in aqueous environment, Physical Chemistry Chemical Physics 18 (2016) 26755–26763. doi:10.1039/C6CP04725D.

[62] M. Allen, D. Tildesley, Computer Simulation of Liquids, Oxford University Press, 1987.

[63] I.-C. Yeh, G. Hummer, System-size dependence of diffusion coefficients and viscosities from molecular dynamics simulations with periodic boundary conditions, Journal of Physical Chemistry B 108 (40) (2004) 15873–15879. doi:10.1021/jp0477147.

[64] D. van der Spoel, P. van Maaren, H. Berendsen, A systematic study of water models for molecular simulation: Derivation of water models optimized for use with a reaction field, The Journal of Chemical Physics 108 (24) (1998) 10220–10230. doi:10.1063/1.476482.

[65] I. M. Svishchev, P. G. Kusalik, Structure in liquid water: A study of spatial distribution functions, The Journal of Chemical Physics 99 (4) (1993) 3049–3058. doi:10.1063/1.465158.

[66] R. Mountain, A. Wallqvist, A collection of results for the spce water model: (1996). doi:10.6028/NIST.IR.5778.

[67] H. Dorrani, A. Mohebbi, A Comparative Study of TIP4P-2005, SPC/E, SPC, and TIP3P-Ew Models for Predicting Water Transport Coefficients Using EMD and NEMD Simulations, Journal of Engineering Thermophysics 32 (2023) 138–161. doi:10.1134/S1810232823010113.

[68] H. Sato, M. Yui, H. Yoshikawa, Ionic diffusion coefficients of Cs^+, Pb^{2+}, Sm^{3+}, Ni^{2+}, SeO_4^{2-} and TcO_4^- in free water determined from conductivity measurements, Journal of Nuclear Science and Technology 33 (12) (1996) 950–955. doi:10.1080/18811248.1996.9732037.

[69] L. Yuan-Hui, S. Gregory, Diffusion of ions in sea water and in deep-sea sediments, Geochimica et Cosmochimica Acta 38 (5) (1974) 703–714. doi:10.1016/0016-7037(74)90145-8.

[70] Y. Iida, T. Yamaguchi, T. Tanaka, Experimental and modeling study on diffusion of selenium under variable bentonite content and porewater salinity, Journal of Nuclear Science and Technology 48 (8) (2011) 1170–1183. doi:10.1080/18811248.2011.9711805.

[71] R.-R. Krüger, W. Abriel, Growth and structure refinement of $CaSeO_4\cdot2H_2O$, Acta Crystallographica Section C: Structural Chemistry 47 (9) (1991) 1958–1959.

10

doi:10.1107/S0108270191002676.

[72] S. Fritz, H. Schmidt, I. Paschke, O. Magdysyuk, R. Dinnebier, D. Freyer, W. Voigt, $CaSeO_4 \cdot 0.625H_2O$ – water channel occupation in a bassanite related structure, Acta Crystallographica Section B 67 (4) (2011) 293–301. doi:10.1107/S0108768111018544.

[73] G. Gatta, U. Hålenius, F. Bosi, L. Cañadillas-Delgado, M. Fernandez-Diaz, Minerals in cement chemistry: a single-crystal neutron diffraction study of ettringite, $Ca_6Al_2(SO_4)_3(OH)_2 \cdot 27H_2O$, American Mineralogist 104 (1) (2019) 73–78. doi:10.2138/am-2019-6783.

[74] R. Allmann, Refinement of the hybrid layer structure $[Ca_2Al(OH)_6]^+ \cdot [1/2 \ SO_4 \cdot 3H_2O]$, Neues Jahrbuch für Mineralogie (1977) 136–144.

[75] M. Khalkhali, X. Ma, H. Zhang, Q. Liu, Bulk and surface properties of gypsum: A comparison between classical force fields and dispersion-corrected dft calculations, Computational Materials Science 164 (2019) 8–16. doi:10.1016/j.commatsci.2019.03.045.

[76] R. K. Mishra, K. Kanhaiya, J. J. Winetrout, R. J. Flatt, H. Heinz, Force field for calcium sulfate minerals to predict structural, hydration, and interfacial properties, Cement and Concrete Research 139 (2021) 106262. doi:10.1016/j.cemconres.2020.106262.

[77] H. Heinz, T.-J. Lin, R. K. Mishra, F. S. Emami, Thermodynamically consistent force fields for the assembly of inorganic, organic, and biological nanostructures: The interface force field, Langmuir 29(6) (2013) 1754–1765. doi:10.1021/la3038846.

[78] P. Kostenetskiy, R. Chulkevich, V. Kozyrev, HPC resources of the Higher School of Economics, Journal of Physics: Conference Series 1740 (2021) 012050.